Special topic paper

Lan Yuan, Zhaoyi Geng, Baoan Fan, Fen Guo* and Chuang Han*

State-of-the-art progress in tracking plasmon-mediated photoredox catalysis

https://doi.org/10.1515/pac-2021-0205

Abstract: Metal nanocrystals (NCs), particularly for plasmonic metal NCs with specific morphology and size, can strongly interact with ultraviolet-visible or even near-infrared photons to generate energetic charge carriers, localized heating, and electric field enhancement. These unique properties offer a promising opportunity for maneuvering solar-to-chemical energy conversion through different mechanisms. As distinct from previous works, in this review, recent advances of various characterization techniques in probing and monitoring the photophysical/photochemical processes, as well as the reaction mechanisms of plasmon-mediated photoredox catalysis are thoroughly summarized. Understanding how to distinguish and track these reaction mechanisms would furnish basic guidelines to design next-generation photocatalysts for plasmon-enhanced catalysis.

Keywords: Characterization; mechanism; metal nanostructure; photocatalysis; plasmon.

Introduction

With the rise of modern civilization, we are walking into an era of energy and environmental crisis, due to the current heavy reliance on fossil fuels and energy-intensive chemical industry [1]. Effective utilization of renewable solar energy for chemical transformations has become extremely necessary for the modern chemical industry [2]. In nature, plants, algae, and certain bacteria can accomplish the solar-to-chemical conversion through photosynthesis. A pioneering study explored by Fujishima and Honda in 1972 showed that the photoexcited charge carriers in TiO_2 semiconductor under ultraviolet (UV) light irradiation could promote the water splitting into H_2 and O_2 [3]. This work inspires us to elaborately design artificial photoredox catalysis systems by implementing similar photochemical processes. Since then, photocatalytic materials based on various semiconductors have widely been examined in photoredox catalysis [4–11].

However, photoredox catalysis based on single-component semiconductors frequently suffers from inefficiency due to the inherent limitations associated with semiconductor materials, such as narrow light response range, rapid charge carrier recombination, insufficient active site for target reaction, etc. [4, 12]. Numerous researches attempt to exploit and develop new materials or strategies to alleviate these issues. The ability of metal nanocrystals (NCs) to trap the photogenerated charge carriers and control light at the sub-wavelength scale has stimulated tremendous interest in constructing metal-semiconductor hybrids.

***Corresponding authors: Fen Guo**, Key Laboratory of Hubei Province for Coal Conversion and New Carbon Materials, School of Chemistry and Chemical Engineering, Wuhan University of Science and Technology, Wuhan 430081, China,
e-mail: guofen@wust.edu.cn; and **Chuang Han**, Department of Chemistry, University of Cincinnati, Cincinnati, Ohio 45221, USA, e-mail: hanch@ucmail.uc.edu
Lan Yuan, Zhaoyi Geng and Baoan Fan, Key Laboratory of Hubei Province for Coal Conversion and New Carbon Materials, School of Chemistry and Chemical Engineering, Wuhan University of Science and Technology, Wuhan 430081, China

Especially, the strong light–matter interaction, unique photoelectric and photothermal effects of plasmonic metal-based composites enable them with great potentials for photoredox catalysis application [8, 9, 13, 14].

Early explorations of the plasmon-mediated solar energy harvesting and conversion were modeled after observing the photosensitive effect of Au and Ag nanoparticles (NPs) [15]. However, in contrast to the long-lived charge carriers generated from dye molecules, the charge carrier's lifetime of plasmonic metal NCs is much shorter, thus resulting in very low photosensitization efficacy based on the traditional hot charge carrier injection mechanism [16]. With the development of material science and characterization technology, several new mechanisms for metal-semiconductor heterojunctions (MSHs)-driven photoredox catalysis have been uncovered [17–20]. Recently, emerging research interest has also been devoted to utilizing the surface plasma resonance (SPR) of single metal NCs without modification of semiconductors for photoredox catalysis, called plasmonic catalysis [21–23]. Nowadays, the explorations of plasmon-mediated photoredox catalysis, including controllable preparation of plasmonic photocatalysts, revealing catalysis mechanisms, and expanding application fields, have become a frontier research topic in the area of solar-to-chemical energy conversion.

Although several working mechanisms of plasmon-mediated photoredox catalysis have been recognized [23, 24], it still remains a challenge to experimentally recognize individual mechanisms and track the intricate light–matter-catalysis interactions. Notably, in recent years, extensive researches have focused on utilizing novel technologies and state-of-the-art characterizations to probe the photophysical/photochemical processes of plasmon-mediated photoredox catalysis [25–29]. The scientific community contributing to this field greatly advances the photocatalytic material design, and reveals the catalytic reaction paths involved in plasmon-enhanced solar-to-chemicals conversion. Differing from previous reviews that mainly focused on the preparation methods, physicochemical properties, working mechanisms, and/or application of plasmonic material, we will present a timely overview of the recent advances in probing and monitoring the reaction mechanisms of plasmon-mediated photoredox catalysis. Various characterization techniques as well as the unique capabilities and limitations of each method are disclosed with typical examples. We also highlight that the significant advances are paralleled with some open issues in this burgeoning field.

Fundamentals of SPR effects and plasmon-mediated photocatalysis

To better understand plasmon-mediated photocatalysis, we should first have a rudimentary understanding of the plasma resonance. The plasmon resonance usually describes the collective response of free charge carriers within metal NCs to the electromagnetic field of incident light [8, 30]. As shown in Fig. 1a, metal NCs possess freely mobile electrons, and that near the surface of metal NCs will be displaced from equilibrium upon photoexcitation, thus suffering from redistribution. During this process, due to the presence of the Coulombic restoring interaction between electrons and the metal nucleus, the electron cloud will collectively oscillate relative to the positive nucleus. When the incident light frequency matches the intrinsic frequency of electron cloud oscillation, the incident light will be absorbed and efficiently coupled with the resonance of electrons. Under such conditions, the phenomenon of SPR will be observed. Since the collective electron oscillations are confined to the surface of metal NCs, SPR primarily refers to localized surface plasmon resonances (L-SPR). It should be noted that in addition to metal NCs, some semiconductors with abound free charge carrier density enabled by chemical doping or post-synthesis can also give rise to SPR [31].

The lifetime of the oscillating electron cloud is in the order of femtosecond, which can relax through different radiative and nonradiative damping processes [8, 23]. In the radiative damping process, the attenuated energy of surface plasmons (SPs) will be converted into photons, while the nonradiative damping leads to the formation of electron-hole pairs by interband and intraband excitation (Fig. 1b) [9, 33]. In detail, upon the plasmon excitation (0 s), Landau damping, a pure quantum mechanical process in which a plasmon quantum is transferred into a single electron-hole pair excitation, occurs within a time scale of a femtosecond (1–100 fs). The induced electric field that represents a time-dependent perturbation on the conduction electrons of the

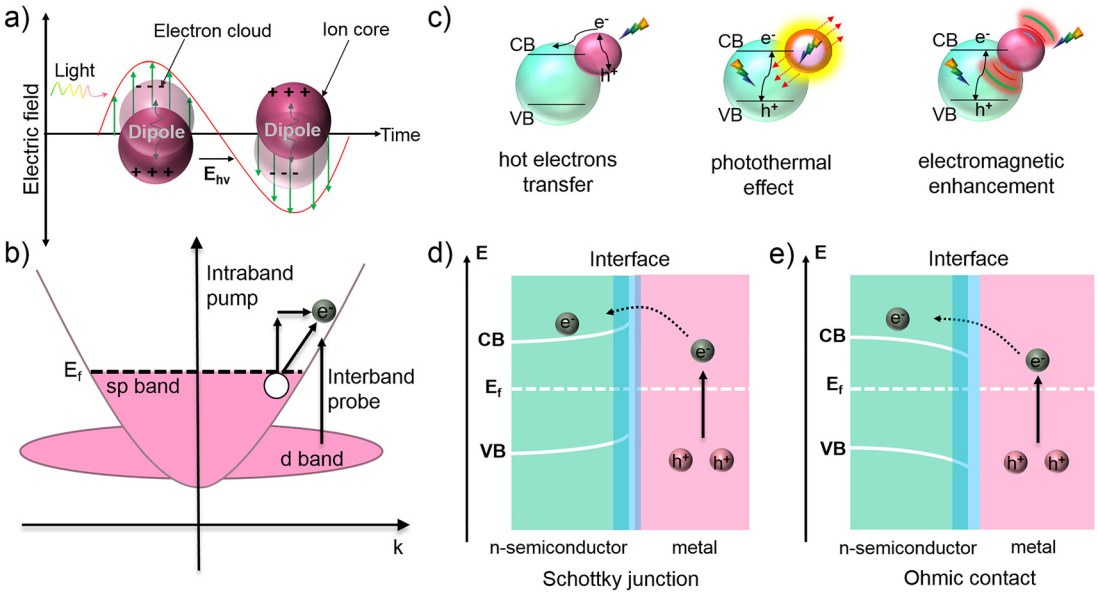

Fig. 1: (a) Schematic illustration of the SPR generation in metal NCs. (b) Fundamental mechanism of plasmon excitation and decay. Reproduced with permission [32]. Copyright 2015 Nature Publishing Group. (c) Diagrams of different mechanisms for SPR-mediated photoredox reactions. Schematic illustrations for the (d) Schottky junction and (e) Ohmic contact between metal and n-type semiconductors.

metal subsequently induce transitions of electrons from occupied to unoccupied states. The electrons with energetic energy (usually called hot electrons, Fig. 1c) can interact with other charge carriers or the lattices of metal NCs, resulting in the energy transfer of the hot electrons to the phonon modes of the NCs. As a consequence, a photothermal process is observed (Fig. 1c), which can increase the temperature of the metal surface and decrease the activation energy of redox reactions [24, 34, 35]. On the other hand, the collective oscillation of electron cloud induces an amplified electromagnetic intensity, which can promote the charge carrier generation and separation in semiconductor, and also favor the activation of absorbed reactants (Fig. 1c) [36].

In addition to the above SPR effects, the interface contacts between metal NCs and other functional components such as semiconductors and organic ligands may also result in the Schottky junction (Fig. 1d) and Ohmic contact effects (Fig. 1e) [37, 38]. Typically, taking the most researched n-type semiconductors for example, when the semiconductor is in contact with the metal, the electrons will flow from the semiconductor into the metal, since the electron work function of the semiconductor is smaller than that of the metal, and a space charge region composed of positively charged and immovable impurity ions is formed on the surface of the semiconductor. The direction of the electric field is directed from the semiconductor to the metal, preventing electrons from continuing to diffuse into the metal. The energy band of the semiconductor at the interface is bent to form a high potential energy zone, which is the Schottky barrier (Fig. 1d). As for Ohmic contact, the energy bands are bending toward the opposite direction as that of the Schottky junction (Fig. 1e). To form a good Ohmic contact, there are two prerequisites: (1) there is a low barrier height between metal and semiconductor, which increases the thermal excitation part in the interface current. (2) The semiconductor has a high concentration of impurity doping, which narrows the semiconductor depletion region, and electrons have more opportunities to tunneling.

Enabled by these heterointerfaces and different working mechanisms, metal NCs provide a powerful platform to mediate photoredox catalysis. Although these effects have been well ground, the question is that for a specific or even a similar reaction system, researchers may have completely different interpretations towards the working mechanism of SPR and metal NCs. This can be ascribed to the fact that the working mechanisms and SPR effects of metal NCs are extremely sensitive to the external dielectric environment. For most cases, some effects usually synthetically affect the photocatalytic behaviors. Recently established in-situ

and ex-situ methods have attracted increasing attention as advisable tools in probing and monitoring the structure and active sites of catalysts, the reaction intermediates as well as the photophysical/photochemical processes involved in catalysis, and thus investigating the reaction and working mechanisms of plasmon-mediated photoredox catalysis. In the following sections, recent advancements in this direction will be thoroughly summarized and discussed.

Recent advances in probing the key processes associated with plasmon-mediated photoredox catalysis

Hot charge carrier generation and distribution

The nonradiative decay of SPs leads to the generation of hot charge carriers, which then initiate the charge-transfer reactions [9, 39]. Since the efficiency of SPR photosensitization is remarkably determined by the non-equilibrium energy level of the hot charge carrier, it is of great essentiality to directly identify and determine the distribution of these carriers, which could enable reasonably predicting their behavior and evaluating their contribution to the catalytic efficiency. In general, the intensity and energy distribution of hot charge carriers can be inferred from theoretically assumed energy distribution or using indirect semi-classical methods, such as SPR frequency shift sensors [40].

To obtain more information about the hot charge carrier generation and attenuation, various spectroscopy and microscopy technologies have been developed. For example, Harutyunyan et al. schemed a double inversion method to extract the data of the pump-probe spectroscopy and directly identified the energy distribution and dynamics of the hot charge carriers in the Au film [32]. Reddy et al. experimentally quantified the steady-state energy distribution of hot charge carriers resorting to a scanning tunneling microscope (STM) [41]. As shown in Fig. 2a, the molecules with appropriate transmission characteristics are carefully chosen to create single-molecule junctions (SMJs) between a plasmonic Au film and the Au tip of an STM. The difference in the measured currents for the cases with and without plasmonic excitation is elucidated to directly quantify the hot charge carrier induced current. It was demonstrated that hot charge carriers were more abundant for a film with thickness of 6 vs. 13 nm due to the Landau damping, which is the dominant physical mechanism of hot charge carrier generation.

There is a growing interest in the detection and visualization of the spatial distribution of hot charge carriers, which requires a more feasible characterization technique with the nanometer spatial resolution. In this regard, the coupling of pump-probe measurements and an STM system affords a strategy to provide the spatial orientation of hot charge carriers with high resolution. Lock et al. employed the technique of STM-induced nonlocal atomic manipulation of adsorbate target molecules on the Si(111) surface to directly observe and control the outcome of injected hot electrons with atomic-scale spatial resolution [42]. This design induces charge injection from the tip of the STM to the adsorbate molecules, and simultaneously records the time-trace of propagated electrons. It shows that the hot carrier-phonon scattering appears within the high-lying 2.0 eV state, and the hot electrons with energy higher than 1.4 eV would directly inject into toluene molecules.

Although the above strategies can furnish fundamental insights into the hot charge carriers generation on plasmonic materials and their energy distribution, it still remains challenging to experimentally and directly identify the hot charge carrier energies during SPR-driven photoredox reaction. Recently, the group of Willets successfully probed the distribution of hot charge carrier generated at Au/TiO_2 substrate based on the scanning electrochemical microscopy (SECM) experiment by employing a variety of molecular probes with different redox potentials [26]. As displayed in Fig. 2b, a Pt ultramicroelectrode (UME, <1 μm) is employed as a tip and positioned close to a region of the substrate. The hole-induced photo-oxidation reaction leads to the conversion of redox molecules from their reduced form (*Red*) to the oxidized form (*Ox*). The current related to the electrochemical oxidation of *Red* at the tip electrode reflects its local concentration change and the

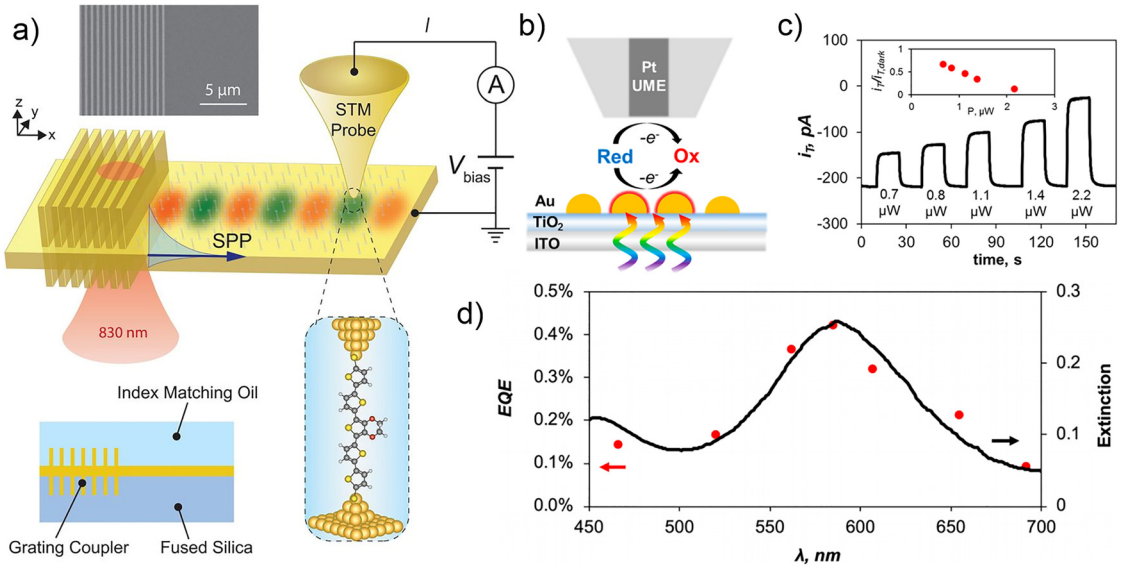

Fig. 2: (a) Schematic of the STM set-up. SMJs are formed between a grounded nanodevice (Au film with integrated grating coupler) and a biased Au STM probe. The bottom left graphic represents a cross-section of the nanodevice covered with index-matching oil. Reproduced with permission [41]. Copyright 2020 American Association for the Advancement of Science. (b) Schematic illustration of an SECM experiment for quantifying the carrier distribution. (c) Tip current (i_T) vs. time trace obtained with an 820 nm radius Pt tip placed 10 μm away from the Au/TiO_2/ITO substrate as 585 ± 18 nm excitation is turned on and off. (d) Action spectra of external quantum efficiencies (EQE) showing the wavelength-dependent hot charge carrier generation. Reproduced with permission [26]. Copyright 2019, American Chemical Society.

photoelectrochemical dynamics at the plasmonic substrate. The experimentally obtained data disclosed that the apparent reaction rate and photocurrent intensity tracks the surface plasmon resonance spectrum of the Au nanoparticles, which indicted the energy distribution of the hot charge carriers (Fig. 2c). The results provide important information for understanding the achievable hot charge carriers generated by MSHs.

Charge carrier transfer and detection

The charge carrier transfer path and dynamics in metal-based heterojunctions have been theoretically analyzed with first-principle calculations [43] and experimentally researched by a series of spectroscopic methods, including transient absorption (TA) spectroscopy [44], surface photovoltage spectroscopy (SPS) [45], electron paramagnetic resonance (EPR) spectroscopy [46], X-ray photoelectron spectroscopy (XPS) [47], ultraviolet-visible (UV-vis) absorption spectroscopy (Abs) [48], photoluminescence (PL) spectroscopy [49], and so on. However, these spectroscopic technologies can only afford photophysical processes of charge carriers without the spatial information [50]. To directly visualize the process of charge carriers transfer in a real catalytic site, more advanced hot charge carrier detection techniques with high spatial and temporal resolution are highly necessary. To this end, several accessible approaches of integrating chemical probes with these spectroscopy have been reported in current literatures, which can be divided into two categories according to the types of the research objects [26, 51–56]. One is the directly photoinduced charge carrier transfer from the metal NCs to the adsorbed molecules. Another is the charge carrier separation at the heterointerface of Schottky junction, Ohmic contact, or multimetallic NCs.

Charge carrier transfer between metal NCs and molecules

The real-time observation based on single-molecule STM technology enables us to measure both photophysical processes of charge carriers and plasmon-induced chemical reaction rates, thus providing insights

into the reaction pathways that cannot be accessed by conventional spectroscopies. Kim et al. employed the STM technique to investigate the plasmon-induced dissociation of the S–S bond in a single dimethyl disulfide molecule adsorbed on Ag(111) and Cu(111) surfaces, using an Ag tip as a plasmonic tip, in real space and real-time [51–53]. They observed that the real-time reaction of the reactant molecules is manifested as a sudden change in the tunneling current (I_t) [53], which is highly sensitive to the change in the gap distance between plasmonic tip and metal surface (Fig. 3a). Figure 3b shows the sudden drop of I_t, which reflects the change in gap distance from $d1$ to $d2$ (Fig. 3a) caused by dissociation of dimethyl disulfide molecule. The STM analyses and DFT calculations jointly reveal that the dissociation of the S–S bond in dimethyl disulfide on Ag(111) or Cu(111) occurred through the direct intramolecular excitation by the plasmons. Later, they applied this technique to the investigation of the plasmon-induced chemical reaction of O_2 molecules that strongly chemisorbed on Ag(110) and found that the dissociation of O_2 is caused by the transfer of hot charge carriers generated through the decay of the plasmons [54]. The results suggest that the reaction mechanism and rate are determined by the electronic structures of plasmonic metal-molecule systems.

Tip-enhanced Raman spectroscopy (TERS) that combines atomic force microscope (AFM) with the surface enhanced Raman scattering (SERS) spectroscopy, is a promising nano-spectroscopic technique to monitor chemical reactions at the nanoscale. Lantman et al. studied the molecule dynamics and chemical reactions for the photocatalyzed conversion of *p*-aminothiophenol (pATP) to *p*,*p*′-dimercaptoazobisbenzene (DMAB) through the TERS technique (Fig. 3c) [55]. The Ag coated AFM tip was used to enhance the Raman signal and act as the catalyst. The tip was placed in contact with a self-assembled pATP molecules adsorbed on Au nanoplates. To record the reaction processes, they employed the 633 nm excitation source to measure Raman signals of reactant molecules, and short periods of 532 nm laser to excite the SPR of Au. The dual-wavelength approach could detect the behaviors of the charge carriers and the photoreaction of pATP separately.

Ren and co-workers employed electrochemical tip-enhanced Raman spectroscopy (EC-TERS) to in situ monitor an SPR-driven decarboxylation, and resolve the spatial transfer and distribution of hot charge carriers with a nanometer spatial resolution [56]. The decarboxylation of 4-mercaptobenzoic acid (4-MBA) molecules

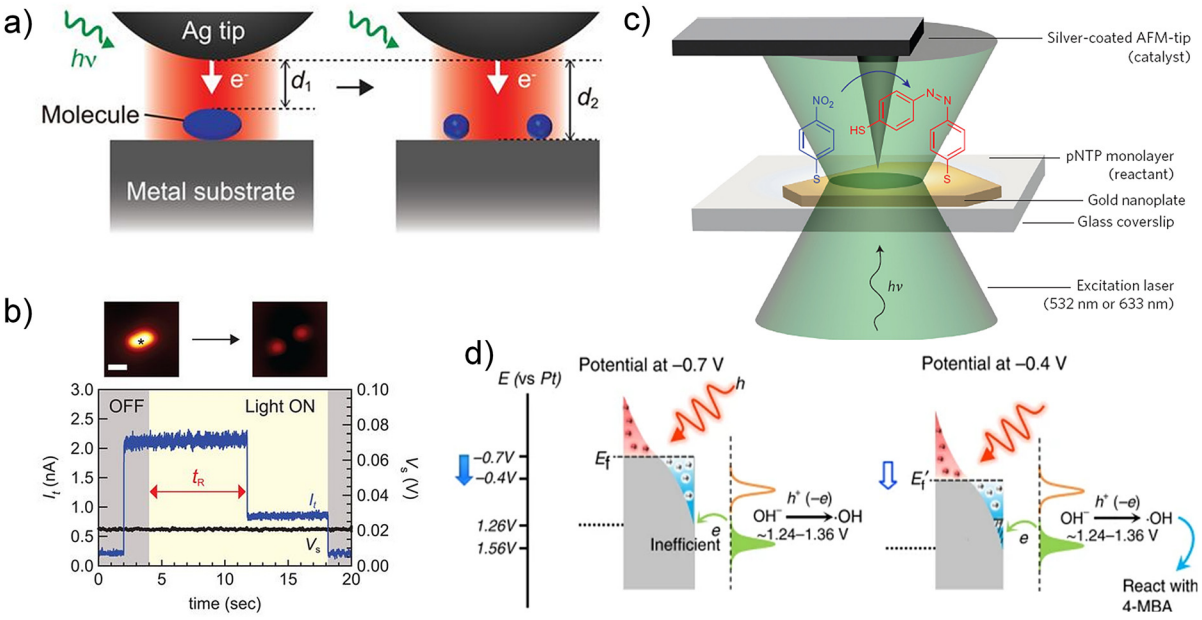

Fig. 3: (a) Schematic illustration of the real-time observation of the plasmon-induced chemical reaction. (b) STM images and corresponding current trace for detecting the dissociation event of dimethyl disulfide molecule on Ag(111) induced by the SPR excited. Reprinted with permission [53]. Copyright 2018 American Association for the Advancement of Science. (c) Schematic overview of the TERS experimental set-up. Reprinted with permission [55]. Copyright 2012 Springer Nature. (d) Schematic illustrating the effect of potential on the carrier energy and the reaction. Reprinted with permission [56]. Copyright 2020 Springer Nature.

was chosen as the model reaction, since 4-MBA has no absorption at the wavelength of the excitation laser (632 nm). By taking advantage of EC-TERS that allows flexible control of the potential, they can further turn on and off the SPR-driven reaction (Fig. 3d). Based on the TERS imaging results, they demonstrated that the transport distance of hot charge carriers is about 20 nm, and the hot charge carriers with a higher energy have a shorter transport distance.

Hot charge carrier transfer at the heterointerface

Ultrafast spectroscopy technologies have been widely employed to probe the charge carrier dynamics of metal-based heterointerface [57, 58]. However, the charge carrier journeys are usually harder to follow, due to the lack of distinct optical fingerprints [44]. Fluorescent probes with non-emitting molecules that become highly emissive after interaction with the specific substrate have been initially used to track the biologically relevant targets due to their high sensitivity. Recently, single-molecule fluorescence spectroscopy based on this type of probe has been successfully applied to explore charge carrier transfer on heterogeneous catalysts. The group of Majima developed new water-soluble and ultrasensitive fluorogenic probes for exploring the interfacial electron transfer reactions on Au deposited TiO_2 NPs [57]. They synthesized a new water-soluble compound of 3,4-dinitrophenyl-boron-dipyrromethene (DN-BODIPY), which has sulfonate groups as fluorophore and dinitrophenyl group as a redox reaction site (Fig. 4a). This probe produces the corresponding fluorescent

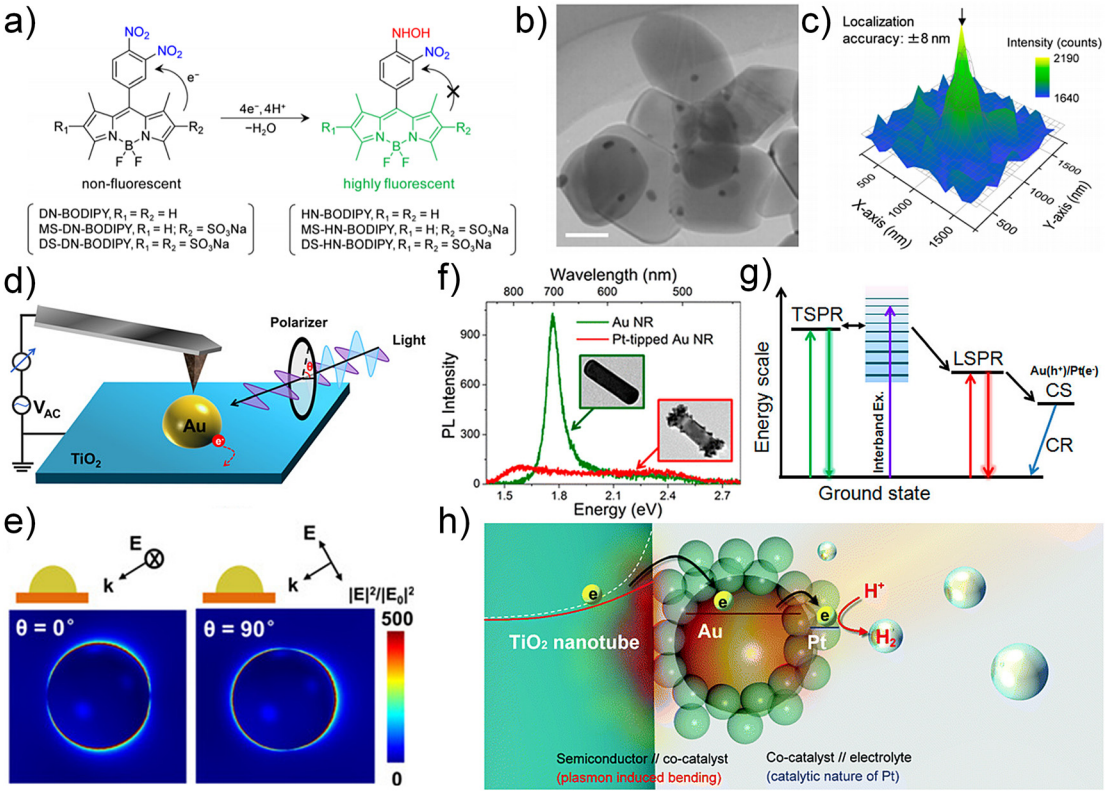

Fig. 4: (a) Schematic illustration of fluorescent probe molecules under ground and excited states. (b) TEM images of 14 nm Au/TiO_2 particles. The scale bars are 100 nm. (c) Fluorescence intensity distribution corresponding to a single product molecule on a 14 nm Au/TiO_2 particle observed in an Ar-saturated DS-DN-BODIPY (50 nm) aqueous methanol solution under 488 nm laser irradiation. Reproduced with permission [57]. Copyright 2013, American Chemical Society. (d) Schematic illustration of the light-irradiated KPFM for imaging the surface potential on a single nanoparticle. (e) Calculated electric field enhancement distribution of Au/TiO_2 nanostructures under polarization angles of 0° and 90°. E_0 is the incident light intensity. Reproduced with permission [59]. Copyright 2020, Wiley. (f) PL intensity of Au NRs and Pt-tipped Au NRs. (g) Schematic diagram for radiative decay of SPs. Reproduced with permission [60]. Copyright 2014, American Chemical Society. (h) Schematic illustration of charge carrier transfer of Au–Pt core-shell NPs modified TiO_2. Reproduced with permission [61]. Copyright 2016, Royal Society of Chemistry.

product via multiple interfacial electron transfer processes between Au and TiO_2 upon light excitation (Fig. 4b and 4c), enabling the investigation of the photoinduced redox reactions over individual Au/TiO_2 NP at the single-molecule levels.

By virtue of the nanometer-scale spatial resolution and sub-millivolt sensitivity in the surface potential, Kelvin probe force microscopy (KPFM) was recently employed to directly image the charge carrier transfer within the real metal-semiconductor NPs. For example, Li and co-workers afforded the experimental evidence of the polarization effect on interfacial charge separation in Au/TiO_2 using the KPFM technology (Fig. 4d) [59]. They observed that as the polarization angle of the excitation light is changed from 0° to 90°, the plasmon-induced surface potential change at the Au/TiO_2 interface progressively enhanced, while the electric field simulation results indicate weakened local near-field that generates less plasmonic electrons in the Au NPs (Fig. 4e). This work quantitatively uncovered the polarization-dependent plasmonic charge density and accumulation at a single-particle level, which is primarily associated with charge injection and separation at the Au/TiO_2 interface, not charge generation. The group of Kim directly observed the charge separation phenomena at the Au/TiO_2 nanotube interfaces under UV light irradiation by KPFM [62]. The surface potential maps of TiO_2 nanotubes with and without Au NPs were monitored on the different substrates (i.e., Si/SiO_2 and Pt substrates). Through direct imaging, it was found that the transferring of electrons from TiO_2 to Au screens the surface potential of TiO_2 nanotubes. By varying the illumination intensity, it was observed that the charged electron number in per Au NP (about 4 nm in diameter) is approximately estimated to be 0.3.

Since every technique has its pristine limitations or disadvantages, the combination of several techniques with complementary aspects allows us to deeply understand the interfacial electron transfer dynamics for individual nanostructures. The group of Majima developed the technique of combining single-particle PL spectroscopy with high-resolution transmission electron microscopy (HR-TEM) to investigate the interfacial electron transfer between Au NRs and Pt cocatalyst [60]. The samples were spin-coated on Al_2O_3/SiO_2-supported TEM grids that were prepared by atomic layer deposition to obtain the corresponding high magnification morphology images. The PL of Au NRs was attributed to the radiative decay of SPs from both the transversal surface plasmon resonance (TSPR) and longitudinal surface plasmon resonance (LSPR). The PL intensity originated from LSPR of the Pt-tipped Au NRs samples is dramatically decreased as compared to bare Au NRs, while the PL intensity corresponding to TSPR is similar for both samples (Fig. 4d). This demonstrates that PL at the LSPR mode is quenched by the tip-coated Pt. Under visible-near infrared (vis-NIR) light irradiation, the hot electrons generated either by TSPR/LSPR excitation or interband excitation transfer to the tip-coated Pt (Fig. 4e), where H^+ is reduced to H_2. The resulting electron-deficient Au NRs oxidize CH_3OH and return to their original metallic state. The spatial separation of reduction and oxidation sites in Pt-tipped Au NRs results in an efficient charge separation (CS), depressed charge recombination (CR), and improved H_2 production rates.

Lately, it has been extensively reported that under certain circumstances, the charge carrier transfer process could also result in the structural reconstruction along with the photoredox reactions [63]. It is therefore highlighted that more attention should be paid to develop operando strategies to in-situ monitor the structural evolution of catalysts that induced by charge carrier transfer [64]. Typically, Chen's group investigated the interfacial charge carrier transfer behaviors at the Ni–Si microwire array junction during photoelectrochemical oxygen evolution reaction (OER) from water, by employing in situ X-ray scattering/diffraction and absorption spectroscopy [65]. They revealed that the in-situ formed adaptive Ni–Si phase with effective barrier height at the heterointerface promoted the photoinduced charge-carrier separation, and thus enhanced the performance of the solar-driven water oxidation. In another work, based on the X-ray absorption spectrum of the Ti L_{III}-edge, they found that the SPR excitation of Au–Pt core-shell NPs could reduce the Schottky barrier between TiO_2 and Pt cocatalyst due to the promoted charge transfer from TiO_2 to the Au–Pt cocatalyst (Fig. 4f) [61].

Enhanced local electromagnetic field and visualization

Irradiating metal NCs with light close to their SPR frequency could result in an intensively enhanced electromagnetic field around the surface of the NCs. It has been reported that the electromagnetic field intensity of

localized "hot spots" can reach 1000-fold as that of the far-field excitation light electromagnetic field intensity, according to the electromagnetic simulations based on the finite-difference time-domain (FDTD) and discrete dipole approximation (DDA) methods [33]. Consequently, the rates of charge carrier generation and separation will be remarkably boosted in these "hot spot" regions. As the electromagnetic field intensity near the surface of metal NCs is significantly enhanced, slight changes in the local environment reflected by the detect technologies, such as PL, fluorescence, or Raman signals of probe molecules, can be greatly amplified and thus enables convenient detection of the electromagnetic field intensity and "hot spot" distribution around metal NCs.

For example, Li's group studied the electric field distributions within the double layer of an atomically flat single-crystal Au(111) electrode with self-assembled probe molecules constructed on it. The result was achieved by Raman spectroscopy through precisely varying the distance of the Raman marker (4′,4-bipyridinium) from the surface of the electrode (Fig. 5a) [66]. Also, a series of "borrowing" strategy, shell-isolated nanoparticle-enhanced Raman spectroscopy (SHINERS), and SHINERS-satellite strategy that developed to overcome the material and morphology limitations in SERS have been summarized [66, 67]. Bhattarai et al. imaged the step edges on an Au(111) surface on the nanoscale by TERS technology using silver AFM tips coated with 4-mercaptobenzonitrile molecules (Fig. 5b) [68]. They observed two-dimensional TERS images that uniquely mapping the electric fields localized at Au(111) step edges with ultrahigh spatial resolution, under 671 nm excitation.

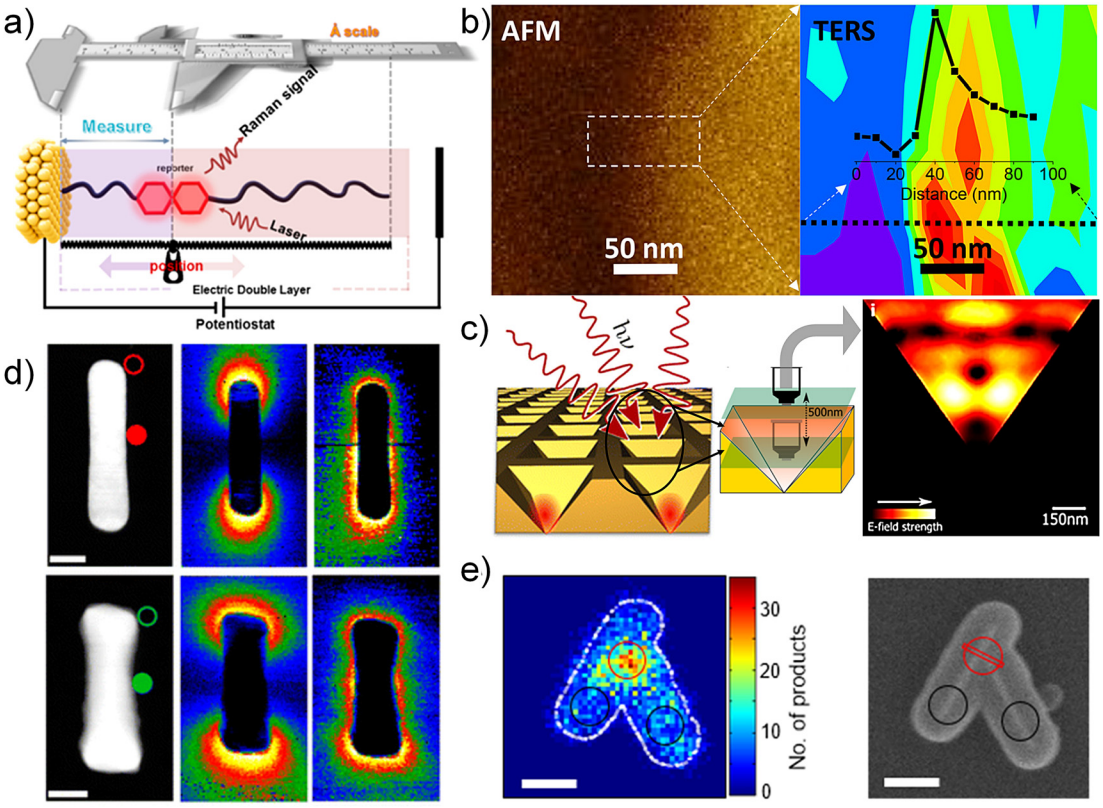

Fig. 5: (a) Schematic illustration of in situ Raman spectroscopy or SERS for probing electromagnetic field distributions. Reprinted with permission [66]. Copyright 2020, American Chemical Society. (b) Correlated AFM (left) and TERS (right) images of a ~2 nm step edge on an Au(111) substrate. Inset shows the data plotted in traces TERS intensity along $Y = 10$ nm at ~1580 cm^{-1}. Reprinted with permission [68]. Copyright 2017, American Chemical Society. (c) Schematic representations of SELM experimental set-up. Reprinted with permission [69]. Copyright 2015, American Chemical Society. (d) STEM images (left), LSP mappings (middle), and TSP mappings (right) of AuNR (up) and HIF-AuNR@AuPd with [100] orientations (down). Scale bars represent 20 nm. Reproduced with permission [28]. Copyright 2013, American Chemical Society. (e) Quantitative super-resolution mapping of catalytic products on a nanostructure (left) and corresponding SEM image of linked Au–Au nanorod encapsulated in SiO_2 (right). Scale bars represent 200 nm. Reprinted with permission [70]. Copyright 2018, American Chemical Society.

Surface enhanced localization microscopy (SELM) opens new possibilities to overcome conventional, diffraction-limited far-field scattering techniques to infer field distributions of nanoscopic plasmons. Kaminski and co-workers demonstrated the direct visualization of electromagnetic fields on patterned metallic substrates at nanometer resolution, using single fluorescent dye (Fig. 5c) [69]. Unlike Raman scatterers, the fluorescence emission of dyes is greatly quenched at the vicinity of metallic substrates, due to the competition between nonradiative decay and field enhancement. Thus, the maximum fluorescence emission, corresponding to minimum field enhancement is observed at a distance away from the surface.

Surface-plasmon (SP) enhanced electromagnetic field on plasmonic nanostructures brings opportunities to increase the catalytic efficiency. To understand the underlying mechanism, quantitative measurements of catalytic enhancement on these nanostructures are required, which is hard to be achieved through single strategy such as the electron microscope or SERS. Han et al. directly visualized the electromagnetic field distributions around Au-based NRs (Fig. 5d) using high-resolution electron microscopy and tomography, by which the electron energy loss spectroscopy (EELS) mapping demonstrated the strong longitudinal electromagnetic field concentrated at the ends and horns of NRs. Moreover, after integrating with SERS technology, this ensemble can serve as a bifunctional platform with high sensitivity to in situ investigate the catalytic reaction kinetics and identify the highly active catalytic sites [28]. Chen's group directly quantified SPR-enhanced catalytic activity within single plasmonic nanostructures at the nanoscale plasmonic hotspots, through integrating the SEM technology with the correlated super-resolution fluorescence microscopy [70]. Figure 5e and 5f respectively shows the plasmonic hotspots at nanoscale gaps on Au–Au and Au–Ag linked nanostructures. Spatially localized higher reaction rate at the gaps vs. non-gap regions indicates the SPR-induced catalytic enhancements, which defined their correlations with the nanostructure geometry and local electric. This work demonstrated the power of this correlative approach in interrogating nanoscale catalytic properties.

Surface temperature measurement

Apart from the redox reaction induced by photogenerated charge carriers, the photothermal effect has also been confirmed to trigger or accelerate certain redox reactions [25]. For example, early in 2009, Park and co-workers experimentally measured the hot electron flow across Pt/TiO_2 Schottky junction by exposing the Pt surface to H_2 and O_2. The measured current during catalytic oxidation of H_2 on the Pt/TiO_2 enhances steadily with the increasing temperature and is proportional to turnover frequency [71]. Yan et al. showed that the Suzuki coupling reactions could be greatly accelerated by the photoexcited Au–Pd NCs through both photocatalysis and photothermal heating. After coating of 25 nm amorphous TiO_x shell on the surface of Au NCs to prevent the photocatalysis process, the reaction rate is significantly decreased over the $Au/TiO_x/Pd$ nanostructures [72]. In another work, Xu and co-workers reported the hierarchical Cu_7S_4@ZIF-8 core@shell nanostructure for accelerating cyclocondensation reaction. In this structure, the Cu_7S_4 hollow microsphere acts as a plasmonic generator for photoheating. The surface temperature could increase up to 94.0 °C under the laser irradiation (1450 nm) with a photothermal conversion efficiency of 31.1 %, which results in 4.5–5.4 fold photoactivity improvement compared to the reaction processed at room temperature [73]. Hong et al. integrated the photothermal and photocatalytic effects of Pd/ZnO for hydrogenation of CO_2 to methanol [74]. They showed that compared with the reactions performed under heating but without light irradiation, the conversion rate is greatly promoted by two-times under irradiation over the temperature range from 190 to 270 °C. It is demonstrated that the photothermal effect induced by the SPR of Pd is the major contributor (>90 %) to the activity enhancement.

Precisely measure the temperature at the surface of plasmonic catalysts is of vital importance to quantify the individual contributions of charge carrier and photothermal effects to the redox catalysis. Optical methods (e.g., infrared spectroscopy, interferometry, fluorescence/luminescence microscopy) and thermometer have been widely employed to measure the temperature of the reaction system. Ho et al. detected the thermal insulation properties of the 3D silica-Au composite gel [14]. As shown in Fig. 6a, the average surface

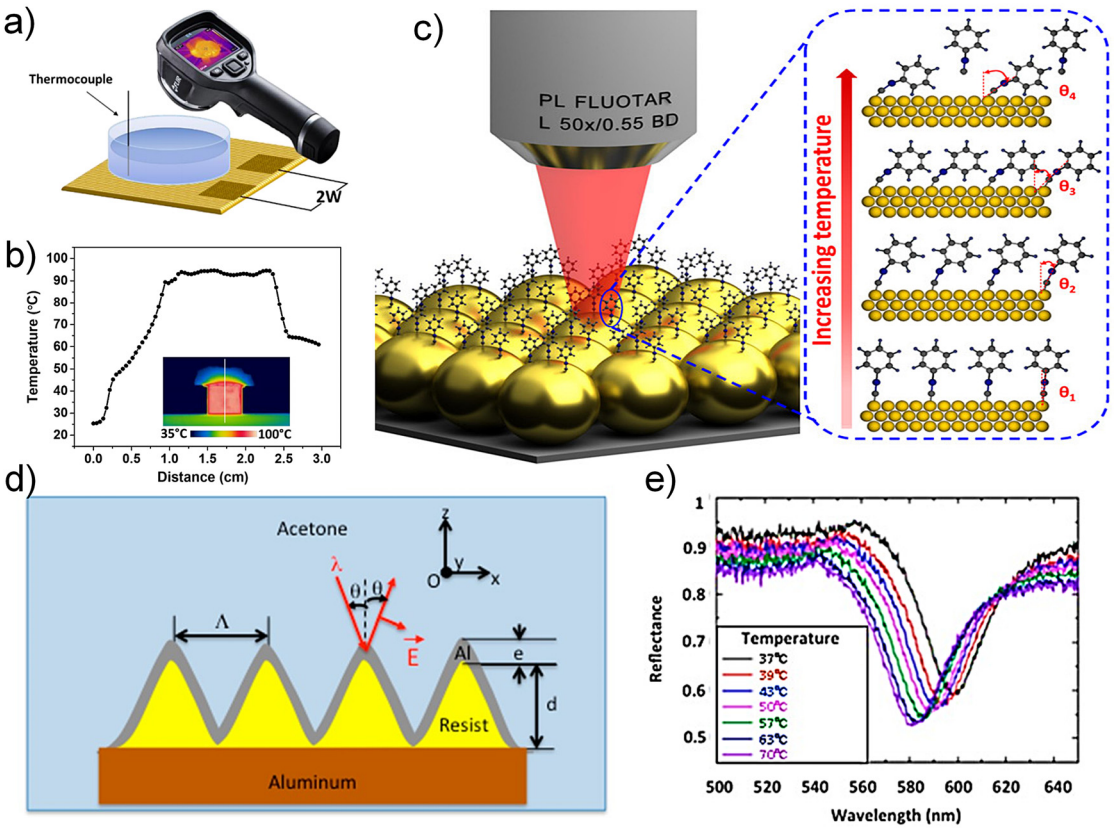

Fig. 6: (a) Schematic of the set-up used for thermal insulation property of silica-Au gel. (b) Line temperature profile with distance from the top of the silica-Au aerogel to the bottom of the heater. Reprinted with permission [14]. Copyright 2018, Wiley. (c) Schematic of temperature-dependent SERS measurement. Reprinted with permission [75]. Copyright 2018, Wiley. (d) Scheme of the temperature-dependent SPR sensors. (e) Experimental SPR spectra measured at different temperatures. Reproduced with permission [76]. Copyright 2019, Multidisciplinary Digital Publishing Institute.

temperature was monitored by an infrared camera, while the bulk water temperature was measured by a thermocouple. They demonstrated that the composite gel in the radial direction shows a temperature difference of about 50 °C between the bottom and the top of the gel (Fig. 6b), revealing the efficient solar-to-heat generation and insulated heat transfer properties of silica-Au composite gel.

However, conventional optical methods and thermometer measured temperature is rather the average temperature. Indeed, the local surface temperature right at the surface of the plasmonic catalysts will be much higher than the average temperature, it is therefore highly desired to accurately in situ measure the local surface temperature at real time. In 2018, Ren's group proposed a method for local temperature sensing using a phenyl isocyanide (PIC) molecule adsorbed on Au NPs by SERS technology [75]. The basis of the method is the good linear relationship between the temperature and N≡C stretching vibration of PIC (Fig. 6c). They demonstrated the temperature-sensing capability for measuring the laser heating effect of the substrate in both air and liquid state for temperature-induced desorption of CO from the Au NP surface. The reliability of this method was validated by the as-obtained accurate desorption temperature compared with that measured by a thermocouple.

Another strategy is to measure the temperature change by analyzing the SPR signature on a metallic surface [76, 77]. The change in the temperature of the metallic surface induces a modification of the local refractive index leading to a shift of the SPR frequency, based on Gaussian function:

$$\lambda_R \approx \Lambda\left(\sqrt{\frac{\epsilon_d \epsilon'_m}{\epsilon_d + \epsilon'_m}} - n_d \sin\theta\right)$$

where λ_R is the SPR wavelength, Λ is the diffraction period, ε_d is the permittivity of the dielectric, ε'_m is the real part of the metal permittivity, θ is the incidence angle on the diffraction grating, and n_d is the refractive index of the dielectric. According to this theory, Jourlin et al. constructed a sensor to detect the temperature at the interface between a solid and a liquid (Fig. 6d) [76]. Metallic Al was selected to prepare this sensor due to its distinct photothermal and plasmonic properties. Figure 6e shows the experimental results obtained from an SPR sensor at different temperatures ranging from 37 to 70 °C. The SPR shifts to smaller wavelengths as the temperature increases. In acetone solvent, the sensitivity of this sensor is 0.387 nm/°C with a response time of 1 ms. This result suggests that the temperature-dependent SPR sensors could be employed as a non-invasive and high-resolution temperature measurement method for metallic surfaces.

Scattering effect and monitor

As aforementioned, radiative properties such as scattering and photoluminescence are straightforwardly related to charge carrier generation and recombination. As the initial step of photoredox catalysis, the light-harvesting ability of metal-based composites greatly affected the density of photogenerated charge carriers and the final overall solar-to-chemical energy conversion efficiency. Notably, plasmonic metal NCs show a promising platform to design photocatalytic materials with tailored light absorption without the bandgap limitations of traditional semiconductor photocatalysts, which usually have a wide bandgap and therefore can only utilize the UV-vis light in the solar irradiation spectrum [78, 79]. Generally, there are two kinds of strategies that can improve the light-harvesting ability of metal-based composites, i.e., expanding the light response region by SPR effect and enhancing light absorption intensity by scattering optical model [80]. The former has been extensively studied and well recognized in photoredox catalysis researches, while the latter has mostly been employed in the solar cell research area [81, 82]. In previous works, the scattering effect usually refers to the extending of light propagation path by metal NCs with a size large than 50 nm [83, 84]. However, Zhang et al. reported the utilization of near-field photon scattering of dielectric environment to intensify the light absorption of small Pt NPs (<10 nm) [85], which provide us with a new exciting and flexible choice to manipulate optical absorption of metal-based composites.

In 2016, Majima and co-workers fabricated a 3D-array consisting of Au nanosphere mono-encapsulated in TiO_2 hollow nanosphere (Au–TiO_2) [86]. The 3D-array shows distinctly enhanced photocatalytic H_2 evolution activity as compared to Au–TiO_2 particulate under both visible and solar light irradiation. FDTD simulation results indicate that the enhanced photoactivity of a 3D array can be ascribed to the elongate light path length due to the multi-scattering between Au–TiO_2 and the inside TiO_2 reflection shell, as shown in Fig. 7a. Recently, we reported a new general strategy of hybridizing SPR with a photon scattering model to realize broadband absorption enhancement of different NPs, including Au, Ag, and Pt NPs [80]. This strategy is resorted to construct a core-shell heterostructure composed of a spherical dielectric core covered with a metal NPs interlayer and tunable TiO_2 shell. As shown in Fig. 7b, this configuration integrates the interfacial photon management, photoexcitation of SPR, and injection of hot charge carriers into one 3D heterojunction. As a result, the enhanced hot charge carrier generation and transfer greatly boost the broad-spectrum light-driven catalysis.

Single-particle dark-field microscopy (DFM) provides an ideal approach to accurately reveal the absorption and scattering spectra of NPs. Typically, Link's group unraveled the intricacies among the morphology, composition, and optical response of bimetallic NCs by single-particle absorption/PL spectroscopy [87]. They demonstrated that the scattering and absorption spectra of blank Au NRs follow the expected trends in peak intensity and location, which can be accurately reproduced by DFT simulations. However, for Pt-decorated Au (Pt–Au) NRs, due to a consequence of coupling between Au and Pt in the hybrid nanostructure, the scattering and absorption spectra are much more unpredictable. In addition, as compared to the PL emission of blank Au, that of Pt–Au NRs is significantly reduced due to the presence of Pt, which indicates that the Au NRs act as an antenna enhancing the generation of hot charge carriers in the catalytically active Pt either through light absorption or charge transfer enhancement.

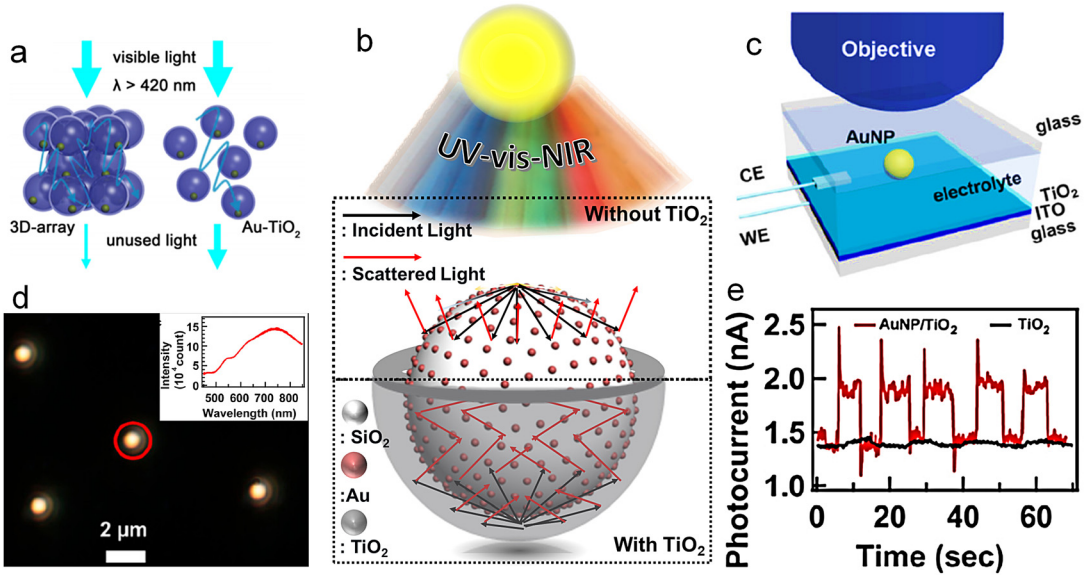

Fig. 7: (a) Illustration of the enhanced photocatalytic activity of 3D-array compared with Au–TiO_2 particulate under visible light irradiation. Reprinted with permission [86]. Copyright 2016, American Chemical Society. (b) Schematic illustration of the interfacial photon management in Au–SiO_2 and Au–SiO_2@TiO_2. Reprinted with permission [80]. Copyright 2018, Royal Society of Chemistry. (c) DFM image of Au NCs (diameter = 237 nm) on the TiO_2/ITO substrate. (d) Schematic illustration of the photoelectrochemical cell. (e) Time evolution of the photocurrent measured on the Au–TiO_2 and bare TiO_2 photoanodes under chopped illumination. Reprinted with permission [88]. Copyright 2020, American Chemical Society.

Recently, Ni and co-workers systematically investigate hot electron response of Au NCs on a TiO_2 photoanode during water splitting using single-particle DFM and photocurrent mapping [88]. As shown in Fig. 7c, the shape and size of the Au NCs were revealed by SEM, and their plasmonic properties were characterized by DFM imaging, by which the scattering spectrum of individual Au NP can be measured. The photoelectrochemical cell was specifically fabricated for the optical microscopic setup (Fig. 7d), based on which the photocurrent was measured and analyzed. Transient photocurrent (Fig. 7e) under chopped illumination exhibits large spikes after turning on the light source, indicating parts of the hot electrons are transferred to the surface of TiO_2. The photocurrent contributed from the single Au NP is about 0.5 nA, whereas nearly zero can be detected from bare TiO_2 under the same condition. They showed that the hot electron injection efficiency (η) can be written in the form as the product of three efficiencies: $\eta = \eta_{abs}\,\eta_{sur}\,\eta_{react}$, where η_{abs} is the efficiency of the absorption of the incident photons, η_{sur} is the efficiency of the surface scattering, and η_{react} is the efficiency of the oxidation reaction. These three parameters are greatly dependent on Au NP's size. Overall, this strategy enables us to directly evaluate the effects of structural parameters and plasmonic properties of the Au NPs on the behaviors of hot electrons.

Summary and outlook

In this review, we thoroughly summarized recent advances of various characterization techniques in probing and monitoring the photophysical/photochemical processes and reaction mechanisms of plasmon-mediated photoredox catalysis. The results from these judicious characterizations undoubtedly give us a preliminary understanding of the stepwise reaction kinetics, possible charge transfer pathways, evolution of active species and intermediates, and reconstruction process of active sites and catalysts. These are crucial information to uncover the catalytic mechanism and construct highly efficient catalysis systems. Given current applications and understandings of these characterization techniques in monitoring plasmon-enhanced catalysis, several challenges and future research directions are proposed and analyzed.

Firstly, as a saying goes, every coin has two sides. Each characterization technique also has its unique capabilities as well as limitations. For example, the most adopted spectrum probing methods show the virtue of time- and/or spatial-resolution ability. But it usually can only offer information about the surface and interface regions. The microscopy (e.g., TEM, SEM, and AFM) technologies are powerful tools to reveal the realistic morphology and structure feedbacks of the catalysts, whereas they apply to a solid surface with a delicate sample preparation process. In addition, the plasmon-enhanced catalysis requires cooperative collection of the light-harvesting, energy and/or charge transfer, and surface reaction in one cycle systems. That is to say, to draw the whole picture of catalytic behaviors, we may need to combinate several approaches or techniques with complementary aspects.

Secondly, understanding the structure-property-catalysis interplays of plasmonic metal-based heterostructures is of great importance to realize the rational design of plasmon-enhanced catalysis systems. Although significant advance in various characterization techniques has been achieved, the underlying charge transfer pathways, plasmon-enhanced mechanism as well as the surface reaction process are still under debate. This is maybe due to the fact that most characterizations are performed under an ex situ state, which however cannot always deliver accurate information because of the contamination, undesired surface change, or structure evolution during the sample preparation, transportation, and characterization. In addition, the existence of short-lived intermediates and fleeting reaction kinetics/thermodynamic states may also be ignored by ex situ experiments. In this regard, the characterization should be performed under the same conditions as practical catalytic operation. Great efforts in developing operando characterizations, which can combine in situ probing with simultaneous measurement of photocatalytic performance is highly desired.

Thirdly, the crystal phase, geometric, and defects of nanomaterials have been considered as the pivotal factors that can greatly influence their properties and performances. However, in contrast to semiconductor-driven photocatalysis, the geometric (e.g., size, morphology, and crystal phase)-dependent and defect-mediated photoactivity of plasmon-mediated catalysis system have not been fully uncovered. In this regard, more efforts should be devoted to seeking feasible approaches to properly regulating the size or optimizing the geometry and crystal phase of the metals that shows different plasmonic behaviors to optimize their applicable photocatalytic performance and atom utilization efficiency, thus further revealing the underlying plasmonic behaviors-photoactivity relationships. Defect engineering such as introducing vacancies into the structure of metals or constructing SPR and non-SPR metal alloys offers a viable strategy to boost the cost- and atom-efficiency of the metal-based photoredox catalytic systems, which deserves future investigations. Moreover, the recent advances of well-developed synthesis methodologies, reliable characterization tools, and unified theoretical calculations provide a great opportunity for us to correlate the relationships among these parameters at the atomic/molecular level.

Last but not least, there is no doubt that advanced characterization and analytical tools facilitate the optimal deployment of next-generation plasmonic photocatalysts. At present, the purchase, installation, utilization, and maintenance of these analytical systems are still expensive. On the one hand, we need to develop smaller, faster, cheaper analytical techniques by reducing system complexity and improving process efficiency. On the other hand, we should strive for the discovery of new synthesis methodologies to access plasmonic photocatalysts with well-defined structures for atomic-level analysis, good stability under operando conditions, and general standardization for analytical reproducibility. Taking together, the key to making progress lies in closing the gap between need and solution by the cooperation among experiment, theory, and industry.

Acknowledgments: The support from the Key Laboratory of Hubei Province for Coal Conversion and New Carbon Materials (Wuhan University of Science and Technology), and the Natural Science Foundation of Hubei Province (2020CFB124, 2020CFB214) is gratefully acknowledged. Lan Yuan and Fen Guo thank the Hubei Provincial Department of Education for the “Chutian Scholar” program.

Research funding: This article was supported by the Key Laboratory of Hubei Province for Coal Conversion and New Carbon Materials (Wuhan University of Science and Technology), and the Natural Science Foundation of Hubei Province (2020CFB124, 2020CFB214) and Hubei Provincial Department of Education by the "Chutian Scholar" program.

References

[1] IEA. World energy outlook 2020, https://www.iea.org/reports/world-energy-outlook-2020.
[2] D. M. Schultz, T. P. Yoon. *Science* **343**, 1239176 (2014).
[3] A. Fujishima, K. Honda. *Nature* **238**, 37 (1972).
[4] C. Han, X. Zhu, J. S. Martin, Y. Lin, S. Spears, Y. Yan. *ChemSusChem* **13**, 4005 (2020).
[5] A. Savateev, M. Antonietti. *ACS Catal.* **8**, 9790 (2018).
[6] C. Han, Y.-H. Li, M.-Y. Qi, F. Zhang, Z.-R. Tang, Y.-J. Xu. *Solar RRL* **4**, 1900577 (2020).
[7] B. M. Hockin, C. Li, N. Robertson, E. Zysman-Colman. *Catal. Sci. Technol.* **9**, 889 (2019).
[8] C. Han, M.-Y. Qi, Z.-R. Tang, J. Gong, Y.-J. Xu. *Nano Today* **27**, 48 (2019).
[9] N. Zhang, C. Han, X. Fu, Y.-J. Xu. *Inside Chem.* **4**, 1832 (2018).
[10] S. Liu, C. Han, Z.-R. Tang, Y.-J. Xu. *Mater. Horiz.* **3**, 270 (2016).
[11] Y. Zhu, Z. Wu, X. Xie, N. Zhang. *Pure Appl. Chem.* **92**, 1953 (2020).
[12] C. Han, Z. R. Tang, J. Liu, S. Jin, Y. J. Xu. *Chem. Sci.* **10**, 3514 (2019).
[13] S. Stewart, Q. Wei, Y. Sun. *Chem. Sci.* **12**, 1227 (2021).
[14] M. Gao, C. K. Peh, H. T. Phan, L. Zhu, G. W. Ho. *Adv. Energy Mater.* **8**, 1800711 (2018).
[15] G. Zhao, H. Kozuka, T. Yoko. *Thin Solid Films* **277**, 147 (1996).
[16] A. Furube, S. Hashimoto. *NPG Asia Mater.* **9**, e454 (2017).
[17] K. Wu, J. Chen, J. R. Mcbride, T. Lian. *Science* **349**, 632 (2015).
[18] X. Huang, H. Li, C. Zhang, S. Tan, Z. Chen, L. Chen, Z. Lu, X. Wang, M. Xiao. *Nat. Commun.* **10**, 1 (2019).
[19] S. K. Cushing, J. Li, F. Meng, T. R. Senty, S. Suri, M. Zhi, M. Li, A. D. Bristow, N. Wu. *J. Am. Chem. Soc.* **134**, 15033 (2012).
[20] J. Li, S. K. Cushing, P. Zheng, T. Senty, F. Meng, A. D. Bristow, A. Manivannan, N. Wu. *J. Am. Chem. Soc.* **136**, 8438 (2014).
[21] U. Aslam, S. Chavez, S. Linic. *Nat. Nanotechnol.* **12**, 1000 (2017).
[22] U. Aslam, V. G. Rao, S. Chavez, S. Linic. *Nature Catal.* **1**, 656 (2018).
[23] E. Cortés, L. V. Besteiro, A. Alabastri, A. Baldi, G. Tagliabue, A. Demetriadou, P. Narang. *ACS Nano* **14**, 16202 (2020).
[24] C. Zhang, T. Kong, Z. Fu, Z. Zhang, H. Zheng. *Nanoscale* **12**, 8768 (2020).
[25] L. Zhou, D. F. Swearer, C. Zhang, H. Robatjazi, H. Zhao, L. Henderson, L. Dong, P. Christopher, E. A. Carter, P. Nordlander, N. J. Halas. *Science* **362**, 69 (2018).
[26] Y. Yu, K. D. Wijesekara, X. Xi, K. A. Willets. *ACS Nano* **13**, 3629 (2019).
[27] E. Cortés. *Science* **362**, 28 (2018).
[28] J. Huang, Y. Zhu, M. Lin, Q. Wang, L. Zhao, Y. Yang, K. X. Yao, Y. Han. *J. Am. Chem. Soc.* **135**, 8552 (2013).
[29] Y. Wang, Y. Ma, X.-B. Li, L. Gao, X.-Y. Gao, X.-Z. Wei, L.-P. Zhang, C.-H. Tung, L. Qiao, L.-Z. Wu. *J. Am. Chem. Soc.* **142**, 4680 (2020).
[30] J. G. Smith, J. A. Faucheaux, P. K. Jain. *Nano Today* **10**, 67 (2015).
[31] A. Agrawal, S. H. Cho, O. Zandi, S. Ghosh, R. W. Johns, D. J. Milliron. *Chem. Rev.* **118**, 3121 (2018).
[32] T. Heilpern, M. Manjare, A. O. Govorov, G. P. Wiederrecht, S. K. Gray, H. Harutyunyan. *Nat. Commun.* **9**, 1 (2018).
[33] W. Hou, S. B. Cronin. *Adv. Funct. Mater.* **23**, 1612 (2013).
[34] F. Yu, C. H. Wang, Y. Y. Li, H. Ma, R. Wang, Y. C. Liu, N. Suzuki, C. Terashima, B. Ohtani, T. Ochiai, A. Fujishima, X. T. Zhang. *Adv. Sci.* **7**, 2000204 (2020).
[35] L. Pan, Y. C. Zhu, Z. Y. Wang, X. Y. Xu, H. C. He, W. Du, J. G. Hu, Y. Zhou. *Sol. RRL* **4** (2020), https://doi.org/10.1002/solr.202000094.
[36] X. Zhou, G. Liu, J. Yu, W. Fan. *J. Mater. Chem.* **22**, 21337 (2012).
[37] S. Bai, J. Jiang, Q. Zhang, Y. Xiong. *Chem. Soc. Rev.* **44**, 2893 (2015).
[38] M. S. Gorji, K. Y. Cheong. *Crit. Rev. Solid State* **40**, 197 (2015).
[39] H.-H. Shin, J.-J. Koo, K. S. Lee, Z. H. Kim. *Appl. Mater. Today* **16**, 112 (2019).
[40] R. Sundararaman, P. Narang, A. S. Jermyn, W. A. Goddard, III, H. A. Atwater. *Nat. Commun.* **5**, 1 (2014).
[41] H. Reddy, K. Wang, Z. Kudyshev, L. Zhu, S. Yan, A. Vezzoli, S. J. Higgins, V. Gavini, A. Boltasseva, P. Reddy, V. M. Shalaev, E. Meyhofer. *Science* **369**, 423 (2020).
[42] D. Lock, K. R. Rusimova, T. L. Pan, R. E. Palmer, P. A. Sloan. *Nat. Commun.* **6**, 8365 (2015).
[43] J. Zhang, M. Guan, J. Lischner, S. Meng, O. V. Prezhdo. *Nano Lett.* **19**, 3187 (2019).
[44] L. Van Turnhout, Y. Hattori, J. Meng, K. Zheng, J. Sá. *Nano Lett.* **20**, 8220 (2020).

[45] X. Q. Ma, X. L. Cui, Z. Q. Zhao, M. A. Melo, E. J. Roberts, F. E. Osterloh. *J. Mater. Chem. A* **6**, 5774 (2018).
[46] J. B. Priebe, J. Radnik, A. J. J. Lennox, M.-M. Pohl, M. Karnahl, D. Hollmann, K. Grabow, U. Bentrup, H. Junge, M. Beller, A. Brückner. *ACS Catal.* **5**, 2137 (2015).
[47] X. Ma, K. Zhao, H. Tang, Y. Chen, C. Lu, W. Liu, Y. Gao, H. Zhao, Z. Tang. *Small* **10**, 4664 (2014).
[48] H. Choi, W. T. Chen, P. V. Kamat. *ACS Nano* **6**, 4418 (2012).
[49] Z. Zhang, Y. Huang, K. Liu, L. Guo, Q. Yuan, B. Dong. *Adv. Mater.* **27**, 5906 (2015).
[50] J. B. Priebe, M. Karnahl, H. Junge, M. Beller, D. Hollmann, A. Brückner. *Angew. Chem. Int. Ed.* **52**, 11420 (2013).
[51] E. Kazuma. *Bull. Chem. Soc. Jpn.* **93**, 1552 (2020).
[52] E. Kazuma, Y. Kim. *Phys. Chem. Chem. Phys.* **21**, 19720 (2019).
[53] E. Kazuma, J. Jung, H. Ueba, M. Trenary, Y. Kim. *Science* **360**, 521 (2018).
[54] E. Kazuma, M. Lee, J. Jung, M. Trenary, Y. Kim. *Angew. Chem. Int. Ed.* **59**, 7960 (2020).
[55] E. M. van Schrojenstein Lantman, T. Deckert-Gaudig, A. J. G. Mank, V. Deckert, B. M. Weckhuysen. *Nat. Nanotechnol.* **7**, 583 (2012).
[56] S.-C. Huang, X. Wang, Q.-Q. Zhao, J.-F. Zhu, C.-W. Li, Y.-H. He, S. Hu, M. M. Sartin, S. Yan, B. Ren. *Nat. Commun.* **11**, 4211 (2020).
[57] T. Tachikawa, T. Yonezawa, T. Majima. *ACS Nano* **7**, 263 (2013).
[58] M. Zhu, X. Cai, M. Fujitsuka, J. Zhang, T. Majima. *Angew. Chem. Int. Ed.* **56**, 2064 (2017).
[59] Y. Gao, W. Nie, Q. Zhu, X. Wang, S. Wang, F. Fan, C. Li. *Angew. Chem. Int. Ed.* **132**, 18375 (2020).
[60] Z. Zheng, T. Tachikawa, T. Majima. *J. Am. Chem. Soc.* **136**, 6870 (2014).
[61] S.-F. Hung, Y.-C. Yu, N.-T. Suen, G.-Q. Tzeng, C.-W. Tung, Y.-Y. Hsu, C.-S. Hsu, C.-K. Chang, T.-S. Chan, H.-S. Sheu, J.-F. Lee, H. M. Chen. *Chem. Commun.* **52**, 1567 (2016).
[62] H. Yoo, C. Bae, Y. Yang, S. Lee, M. Kim, H. Kim, Y. Kim, H. Shin. *Nano Lett.* **14**, 4413 (2014).
[63] Y. Zhu, J. Wang, H. Chu, Y.-C. Chu, H. M. Chen. *ACS Energy Lett.* **5**, 1281 (2020).
[64] S.-F. Hung. *Pure Appl. Chem.* **92**, 733 (2020).
[65] C.-W. Tung, T.-R. Kuo, C.-S. Hsu, Y. Chuang, H.-C. Chen, C.-K. Chang, C.-Y. Chien, Y.-J. Lu, T.-S. Chan, J.-F. Lee, J.-Y. Li, H. M. Chen. *Adv. Energy Mater.* **9**, 1901308 (2019).
[66] B.-Y. Wen, J.-S. Lin, Y.-J. Zhang, P. M. Radjenovic, X.-G. Zhang, Z.-Q. Tian, J.-F. Li. *J. Am. Chem. Soc.* **142**, 11698 (2020).
[67] H. Zhang, S. Duan, P. M. Radjenovic, Z.-Q. Tian, J.-F. Li. *Acc. Chem. Res.* **53**, 729 (2020).
[68] A. Bhattarai, A. G. Joly, W. P. Hess, P. Z. El-Khoury. *Nano Lett.* **17**, 7131 (2017).
[69] C. Steuwe, M. Erdelyi, G. Szekeres, M. Csete, J. J. Baumberg, S. Mahajan, C. F. Kaminski. *Nano Lett.* **15**, 3217 (2015).
[70] N. Zou, G. Chen, X. Mao, H. Shen, E. Choudhary, X. Zhou, P. Chen. *ACS Nano* **12**, 5570 (2018).
[71] A. Hervier, J. R. Renzas, J. Y. Park, G. A. Somorjai. *Nano Lett.* **9**, 3930 (2009).
[72] S. Xie, Y. Wang, Q. Zhang, W. Fan, W. Deng, Y. Wang. *Chem. Commun.* **49**, 2451 (2013).
[73] F. Wang, Y. Huang, Z. Chai, M. Zeng, Q. Li, Y. Wang, D. Xu. *Chem. Sci.* **7**, 6887 (2016).
[74] D. Wu, K. Deng, B. Hu, Q. Lu, G. Liu, X. Hong. *ChemCatChem* **11**, 1598 (2019).
[75] S. Hu, B.-J. Liu, J.-M. Feng, C. Zong, K.-Q. Lin, X. Wang, D.-Y. Wu, B. Ren. *J. Am. Chem. Soc.* **140**, 13680 (2018).
[76] J. Ibrahim, M. Al Masri, I. Verrier, T. Kampfe, C. Veillas, F. Celle, S. Cioulachtjian, F. Lefèvre, Y. Jourlin. *Sensors* **19**, 3354 (2019).
[77] W. Luo, R. Wang, H. Li, J. Kou, X. Zeng, H. Huang, X. Hu, W. Huang. *Opt. Express* **27**, 576 (2019).
[78] C. Han, Q. Quan, H. M. Chen, Y. Sun, Y.-J. Xu. *Small* **13**, 1602947 (2017).
[79] S. Sun, H. Liu, L. Wu, C. E. Png, P. Bai. *ACS Catal.* **4**, 4269 (2014).
[80] C. Han, S.-H. Li, Z.-R. Tang, Y.-J. Xu. *Chem. Sci.* **9**, 8914 (2018).
[81] S. Son, S. H. Hwang, C. Kim, J. Y. Yun, J. Jang. *ACS Appl. Mater. Interfaces* **5**, 4815 (2013).
[82] N. Eldabagh, M. Micek, A. E. DePrince, J. J. Foley. *J. Phys. Chem. C* **122**, 18256 (2018).
[83] M. Murdoch, G. Waterhouse, M. Nadeem, J. Metson, M. Keane, R. Howe, J. Llorca, H. Idriss. *Nat. Chem.* **3**, 489 (2011).
[84] T. J. Norman, C. D. Grant, D. Magana, J. Z. Zhang, J. Liu, D. Cao, F. Bridges, A. Van Buuren. *J. Phys. Chem. B* **106**, 7005 (2002).
[85] N. Zhang, C. Han, Y.-J. Xu, J. J. Foley IV, D. Zhang, J. Codrington, S. K. Gray, Y. Sun. *Nat. Photonics* **10**, 473 (2016).
[86] X. Shi, Z. Lou, P. Zhang, M. Fujitsuka, T. Majima. *ACS Appl. Mater. Interfaces* **8**, 31738 (2016).
[87] A. Joplin, S. A. Hosseini Jebeli, E. Sung, N. Diemler, P. J. Straney, M. Yorulmaz, W.-S. Chang, J. E. Millstone, S. Link. *ACS Nano* **11**, 12346 (2017).
[88] H. Zhu, H. Xie, Y. Yang, K. Wang, F. Zhao, W. Ye, W. Ni. *Nano Lett.* **20**, 2423 (2020).